J. Fluid Mech. (2000), *vol.* 422, *pp.* 319–346. Printed in the United Kingdom

Reynolds-number scaling of the flat-plate turbulent boundary layer

By DAVID B. DeGRAAFF AND JOHN K. EATON

Department of Mechanical Engineering, Stanford University, Stanford, CA 94305, USA

(Received 21 September 1999 and in revised form 2 June 2000)

Despite extensive study, there remain significant questions about the Reynolds-number scaling of the zero-pressure-gradient flat-plate turbulent boundary layer. While the mean flow is generally accepted to follow the law of the wall, there is little consensus about the scaling of the Reynolds normal stresses, except that there are Reynolds-number effects even very close to the wall. Using a low-speed, high-Reynolds-number facility and a high-resolution laser-Doppler anemometer, we have measured Reynolds stresses for a flat-plate turbulent boundary layer from $Re_\theta = 1430$ to 31 000. Profiles of $\overline{u'^2}$, $\overline{v'^2}$, and $\overline{u'v'}$ show reasonably good collapse with Reynolds number: $\overline{u'^2}$ in a new scaling, and $\overline{v'^2}$ and $\overline{u'v'}$ in classic inner scaling. The log law provides a reasonably accurate universal profile for the mean velocity in the inner region.

1. Introduction

Modern turbulent-boundary-layer calculation methods must use turbulence models, since direct numerical simulation of the Navier–Stokes equations is well beyond the reach of present day computers except at very low Reynolds numbers. Model developers must rely on the experimental database to formulate and validate new models. Unfortunately, because of the expense of large-scale facilities, and the difficulty in accurately measuring high-Reynolds-number flows, the vast majority of available data have been acquired at low Reynolds numbers. Because most applications of engineering interest are at much higher Reynolds numbers, it is critical to understand the dependence of the flow on Reynolds number.

The over-arching goal of our research program is to study non-equilibrium boundary-layer scaling with Reynolds number. To that end, it is an essential starting point to define an equilibrium boundary layer. It should be noted that the phrase 'equilibrium layer' was used by Townsend (1961) to mean a region of a boundary layer where the local rates of energy production and dissipation are equal, and the phrase 'equilibrium boundary layer' has been used to mean that $U_e \sim x^a$ (U_e is the velocity at the edge of the boundary layer), or that $\delta^*/\tau_w(\mathrm{d}p/\mathrm{d}x)$ equals a constant (δ^* is the boundary-layer displacement thickness), or that the velocity defect profiles have attained complete similarity (Bradshaw 1967). These definitions include variously configured adverse pressure gradient and constant shear stress boundary layers, and may or may not encompass the zero-pressure-gradient boundary layer. Here, we are using a narrower, but perhaps more applicable definition: an equilibrium boundary layer is a wall-bounded flow where the shear stress distribution is in equilibrium with the shear stress at the wall. This is an equilibrium in the sense that it is the state that an unperturbed two-dimensional boundary layer will naturally attain, and it is the state that a perturbed boundary layer will revert to once the perturbation, e.g. curvature or

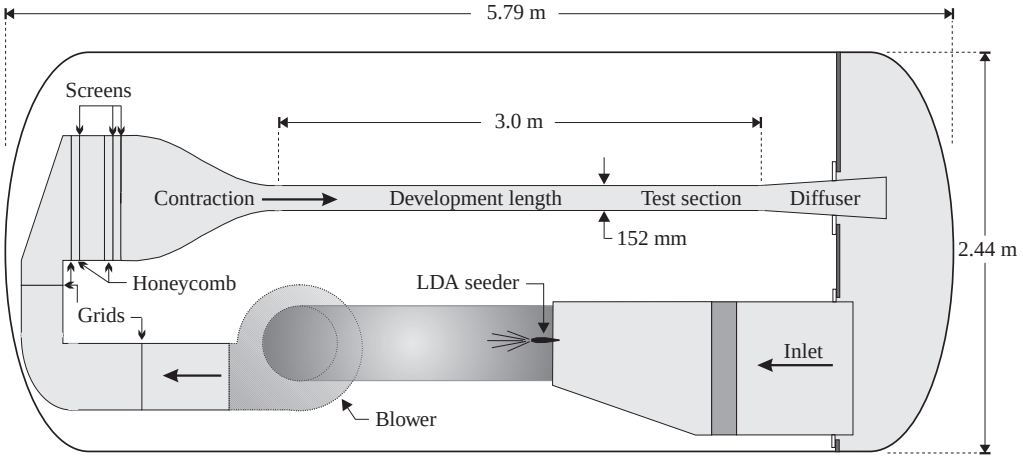

FIGURE 1. Side view of the pressure vessel and wind tunnel.

Re_θ	U_e (m s^{-1})	δ (mm)	θ (mm)	Δ (mm)	H	G	$K \times 10^6$	Symbol
1430	6.04	31.25	3.69	118	1.43	6.72	0.11	△
2900	9.83	37.93	4.54	153	1.38	6.79	0.06	◇
5200	18.95	35.87	4.19	149	1.36	6.92	0.03	○
13 000	14.36	34.56	3.78	139	1.31	6.57	0.01	●
31 000	17.15	35.58	3.66	139	1.27	6.37	0.00	□

TABLE 1. Flat-plate profiles: outer variables, integral parameters, and pressure gradient parameters. Note: δ is 'δ_{99}', and Δ is the Clauser–Rotta lengthscale, $\delta^* U_e/u_\tau$.

pressure gradient, is removed. The equilibrium-boundary-layer concept will provide a framework for our study of perturbed boundary layers, and lead to methods for prediction and scaling of high-Reynolds-number non-equilibrium boundary layers.

The goal of this paper is to quantify the equilibrium turbulent boundary layer by measuring and scaling the mean flow and the Reynolds stresses over a large Reynolds-number range. For clarity, each flow quantity is discussed in a separate section. Each section starts with a brief literature review, then presents our own results, and concludes with a discussion.

2. Facility and experimental techniques

A new facility was built for this study, consisting of a laboratory-scale wind-tunnel entirely enclosed in a pressure vessel. The Reynolds number can be varied by a factor of 8 by changing the ambient density, and an additional factor of 3 by changing the free-stream velocity, resulting in a total Reynolds-number range of approximately 24 : 1. This facility allows independent variation of the Reynolds number, since the Mach number is always below 0.05, and the boundary-layer thickness at a given position is approximately constant (see table 1).

A side view of the pressure vessel and wind tunnel is shown in figure 1. Increasing the ambient pressure in and around the wind tunnel by enclosing it in a pressure vessel allows standard wind-tunnel construction of wood and Plexiglas. This is economical, and makes the experiment easy to modify. The pressure vessel supports 8 atmospheres,

and has a hinged end-bell which provides access to the entire inner diameter. When this door is closed, the wind tunnel becomes a semi-sealed closed circuit, which keeps the laser-Doppler anemometer (LDA) seed particles recirculating. Starting with the return leg in the lower right hand side of figure 1, the air passes through a heat exchanger, and then enters a flexible duct to direct it into the blower. At the entrance of the duct, an air-brush sprays a fine water mist to introduce 0.45 μm diameter polystyrene spheres into the air for LDA seed. After the blower, the air passes through flow-conditioning screens, grids, and honeycombs, and then a 5 : 1 contraction, before entering the development length. The test section is 152 mm high, by 711 mm wide, with a free-stream turbulence level of 0.2%.

With the exception of the lowest-Reynolds-number case, the boundary layer was tripped 150 mm downstream of the contraction, using a plastic rectangle which was 1.6 mm high, and extended 6.4 mm in the streamwise direction. This results in a development length of 1500 trip heights before the location where the flat-plate profiles are measured. For the lowest-Reynolds-number case ($Re_\theta = 1430$), a suction slot was used to start a new boundary layer 400 mm downstream of the contraction, and a trip was placed 250 mm further downstream. The profile was taken 1020 trip heights downstream of the trip.

The flat-plate boundary layer was measured on the floor of the wind tunnel, along the centreline of the test section. The tunnel has a constant cross-sectional area, so the boundary-layer growth results in a slightly favourable pressure gradient, making these boundary layers not truly zero-pressure-gradient boundary layers. Table 1 shows the acceleration parameter,

$$K = \frac{\nu}{U_e^2} \frac{\mathrm{d}U_e}{\mathrm{d}x}, \tag{2.1}$$

which indicates the acceleration is insignificant for the $Re_\theta = 2900$ case and above, and very small for the $Re_\theta = 1430$ case. Note that substantial deviation from the log law occurs only for $K > 1.6 \times 10^{-6}$ (Patel 1965).

The goal of this experiment is to measure high-Reynolds-number turbulence, so a measurement system with sufficient spatial resolution is necessary. This required development of a custom-built two-component high-resolution LDA. This LDA forms a measurement volume with three beams which are frequency-shifted differently, and then extracts two-component velocity information from each Doppler burst using a Fourier transform. Extensive design details, qualification experiments, and uncertainty analysis are given in DeGraaff & Eaton (2000), with further details in DeGraaff (1999).

By focusing the beams to very narrow waists, and using side-scatter collection optics, we were able to attain a measurement volume 35 μm in diameter, and 60 μm in length. These dimensions were measured directly, since simple lens formula predictions break down when real lens effects (e.g. manufacturing tolerances, spherical abberation) and Gaussian beam optics determine the actual beam waist sizes. Resolution issues and comparisons to hot-wires and cross-wires will be discussed below along with the turbulence measurements.

A summary of the uncertainty analysis for the LDA measurements is shown in table 2 (from DeGraaff & Eaton 2000). The turbulence quantity uncertainties vary greatly when presented as a percentage of their local value, since the quantities go to zero at the wall. The values listed in table 2 are uncertainties in the centre of the profiles, where the uncertainties are a fairly constant percentage of their local values. This table provides a general guideline for examining velocity profiles, noting that near-wall uncertainties are generally higher.

U	$\pm 1.5\%$
$\overline{u'^2}$	$\pm 4\%$
$\overline{v'^2}$	$\pm 8\%$
$\overline{u'v'}$	$\pm 10\%$

TABLE 2. Uncertainty guidelines.

Except where explicitly noted (figure 11 only), all velocity data were measured with the high-resolution LDA system.

3. Results and discussion

3.1. *Streamwise mean velocity*

Perhaps the most celebrated analytical result in fluid dynamics is the law of the wall. This derives from the argument that once the surface shear stress is determined, the flow near a smooth wall depends only on the distance to the wall and the fluid properties. This assumes that the only effect of the boundary-layer edge velocity and boundary-layer thickness, as well as overall geometry and upstream history, is to determine the wall shear stress (Bradshaw & Huang 1995). This leads directly to the expression

$$U^+ = F_1(y^+), \tag{3.1}$$

or equivalently (Rotta 1962; Landau & Lifshitz 1987),

$$\frac{\partial U}{\partial y} = \frac{u_\tau}{y} F_2(y^+), \tag{3.2}$$

where

$$U^+ \equiv \frac{U}{u_\tau}, \tag{3.3}$$

$$y^+ \equiv \frac{y u_\tau}{\nu}, \tag{3.4}$$

and

$$u_\tau \equiv \sqrt{\frac{\tau_w}{\rho}}. \tag{3.5}$$

In the very near-wall region, the viscosity dominates, and (3.1) becomes

$$U^+ = y^+. \tag{3.6}$$

Further from the wall, we expect that viscosity plays a negligible role, and $F_2(y^+)$ (equation (3.2)) is simply a constant (defined to be $1/\kappa$). Equation (3.2) can then be integrated to give the logarithmic law of the wall, or 'log law':

$$U^+ = \frac{1}{\kappa} \ln y^+ + B. \tag{3.7}$$

This result can also be derived more generally using asymptotic expansions (Tennekes & Lumley 1972). The log law has proved to be an effective universal curve for the mean velocity profile in the inner region of the flat-plate turbulent boundary layer, generally defined as $y/\delta < 0.2$ (δ will be understood to mean δ_{99}: the height where the velocity is 99% of the free-stream velocity). Only recently have doubts about its

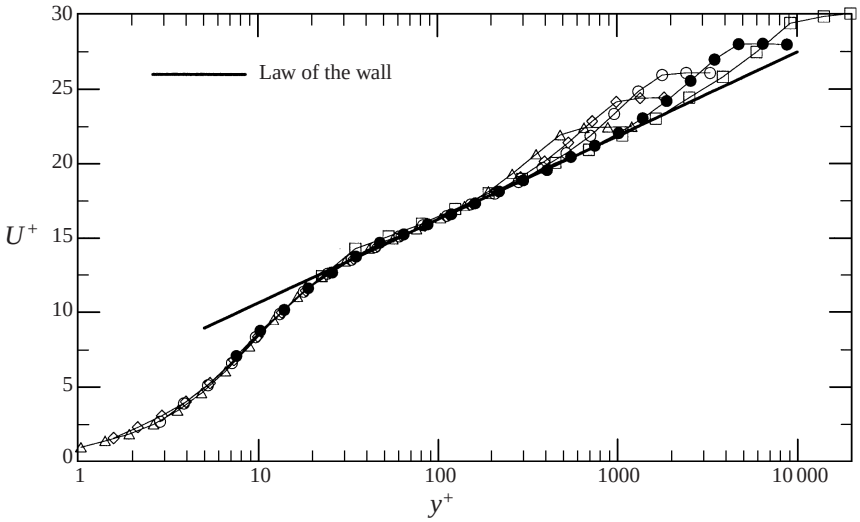

FIGURE 2. Flat-plate mean streamwise velocity. Symbols in table 1.

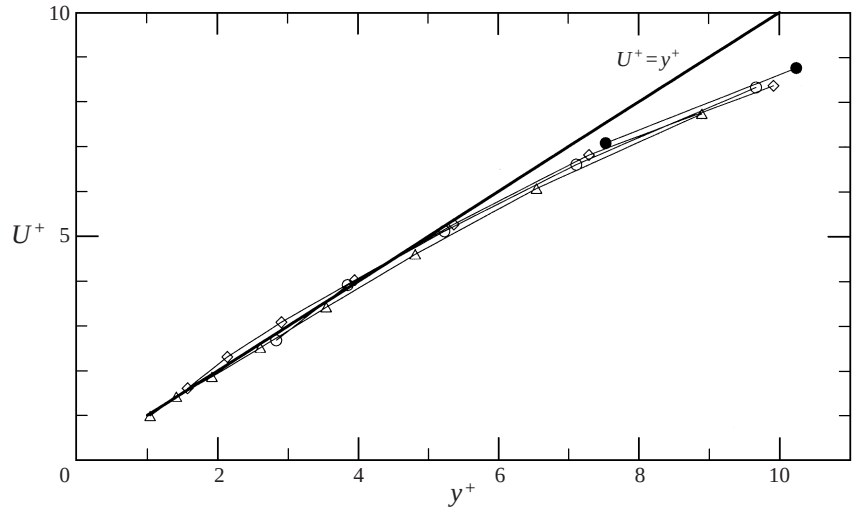

FIGURE 3. Flat-plate mean streamwise velocity: sublayer. Symbols in table 1.

validity begun to arise. The question is whether the log law is really Reynolds-number independent, and whether a power law with Reynolds-number dependence would be more correct (Barenblatt 1993; George & Castillo 1997; Zagarola, Perry & Smits 1997). With the exception of a few objectors, however, the log law is still generally accepted as the universal profile of the mean velocity in the inner region of the turbulent boundary layer, and it is an integral part of many turbulence models. It should be noted that experimental uncertainty in the available data, and the restricted Reynolds-number range of most experiments, have precluded the selection of the best profile model on a purely empirical basis.

Mean profiles are shown in inner coordinates in figure 2. There is good agreement with the law of the wall from $y^+ = 50$ to $y/\delta = 0.2$, and good agreement with $U^+ = y^+$ below $y^+ = 4$. A closeup of the near-wall region is shown in figure 3.

Re_θ	u_τ (m s^{-1})	ν/u_τ (μm)	$C_f/2 \times 10^3$	τ_w (Pa)	$\Delta U/u_\tau$
1430	0.269	57.8	1.98	0.086	1.89
2900	0.403	38.2	1.68	0.193	2.32
5200	0.727	21.2	1.47	0.629	2.67
13 000	0.512	7.97	1.27	1.207	2.34
31 000	0.573	3.55	1.12	3.033	2.15

TABLE 3. Flat-plate profiles: log law fit results.

Unfortunately, these data cannot provide definitive answers to the questions regarding the validity of the law of the wall, because we derived the wall shear stress from a best fit to the log law between $y^+ = 50$ and $y/\delta = 0.2$, using the Coles log law constants: $\kappa = 0.41$ and $B = 5.0$. This method is equivalent to using a Preston tube or any other device which relies on the existence of a law of the wall (Bradshaw & Huang 1995). The inner scales resulting from this fit are shown in table 3.

Although it would be circular to attempt to prove the law of the wall with data that is scaled by fitting the law of the wall, there are two independent confirmations which suggest that u_τ is well estimated by the log law fit. As figure 3 shows, the measurements of U^+ vs. y^+ in the sublayer agree very closely with the prediction $U^+ = y^+$. Also, looking ahead to figure 25, the total shear stress is equal to u_τ^2 near the wall within experimental uncertainty. These data indicate two things: that the law of the wall is fairly accurate over this Reynolds-number range, and that any attempt to 'prove' or 'disprove' the law of the wall in an external boundary layer will need to measure the wall shear stress extremely accurately in order to see any significant differences.

A brief study was made to determine the best log law constants from these five profiles. The value of κ was varied from 0.39 to 0.45, and B was allowed to float to minimize the error. The quality of the fit, as evaluated by the mean square differences between the data and the log law, was essentially constant for the different values of κ. It is evidently not possible to define a best κ and B when the wall shear stress is not known independently.

For the purpose of finding self-similar profiles, the boundary layer must be divided into the inner and outer layers (Townsend 1956). In the outer layer, the flow is assumed to be independent of viscosity, and the wall shear stress acts only to prescribe a near-wall velocity needed for matching with the inner layer. Outer scales depend on the global properties of the flow, e.g. δ and U_e. The proper scaling is generally considered to be

$$\frac{U_e - U}{u_\tau} = F_3\left(\frac{y}{\delta}\right), \tag{3.8}$$

and is known as the velocity defect law (Clauser 1956). These data are plotted in defect coordinates in figure 4. The profiles are well collapsed throughout the outer region of the boundary layer. The function F_3 must also take the form of a logarithm in any region of overlap with the log law of the inner layer, giving the form

$$\frac{U_e - U}{u_\tau} = -\frac{1}{\kappa}\ln\frac{y}{\delta} + C. \tag{3.9}$$

This can be expressed as a composite expansion in two different lengthscales, to give

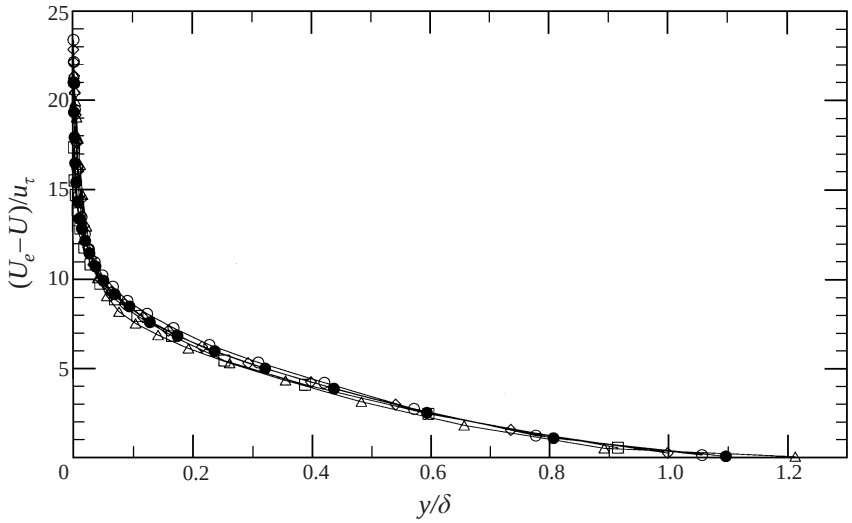

FIGURE 4. Flat-plate mean streamwise velocity in deficit coordinates. Symbols in table 1.

the law of the wall plus the law of the wake of Coles (1956):

$$U^+ = F_1(y^+) + \frac{\Pi}{\kappa} W\left(\frac{y}{\delta}\right). \tag{3.10}$$

While the universality of the law of the wall is rarely questioned, the universality of the law of the wake is somewhat in doubt. Analysing all available data, Coles (1962) concluded that the wake parameter, $\Delta U/u_\tau$ asymptotes to a constant value for $Re_\theta > 6000$. Later experiments, however, have indicated that the wake parameter starts to decrease for $Re_\theta > 15\,000$ (Mabey 1979; Fernholz & Finley 1996; Gad-el-Hak & Bandyopadhyay 1994). A slow decrease in the wake parameter at high Reynolds number is also predicted by the closure model of Perry, Marusic & Li (1994), which relates the shear stress distribution to the streamwise rate of change of the wake parameter. Note that their definition of an equilibrium boundary layer is $\mathrm{d}(\Delta U/u_\tau)/\mathrm{d}x = 0$, and, hence, a zero-pressure-gradient boundary layer is a 'quasi-equilibrium' boundary layer in their terminology.

This slow decrease at high Reynolds number is evident in figure 5. The solid circles should be compared with the Coles fit, since these log law constants are the same as those used by Coles (1956). The open circles are derived from the Zagarola *et al.* (1997) log law constants, and the open diamonds are from the log law constants of Osterlund (1999). Although the magnitude of the wake parameter is a strong function of the log law constants, all three sets of constants show a rapid increase for $Re_\theta < 6000$, followed by a slight drop between $Re_\theta = 6000$ and 12 000. At very high Reynolds number, the Osterlund constants result in a constant wake parameter, while the Coles and Zagarola constants give a wake parameter which continues to decrease. If $\Delta U/u_\tau$ continues to drop with increasing Reynolds number, then the law of the wake is not universal, even at high Reynolds number. This could be explained by changes in the outer layer owing to slowly varying $\mathrm{d}\delta/\mathrm{d}x$ or $\delta/u_\tau(\mathrm{d}u_\tau/\mathrm{d}x)$ with increasing Reynolds number. A decrease could also be explained by log law constants which are functions of Reynolds number, i.e. a failure of the log law to correctly collapse the inner region. Note that the uncertainty of the wake parameter due to the uncertainty in the velocity is $\pm 3\%$.

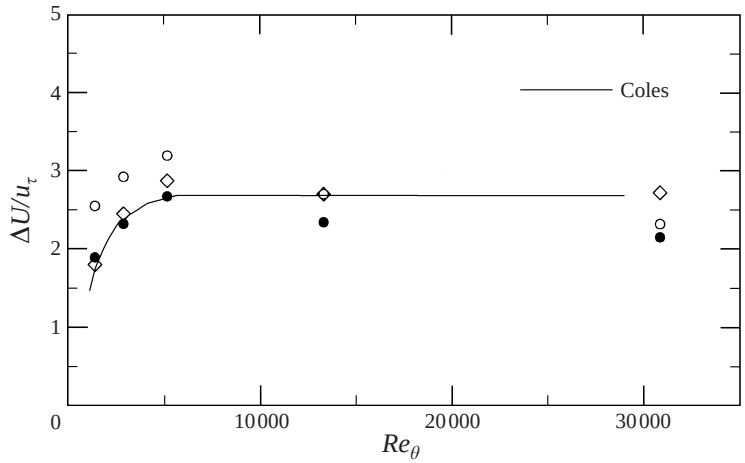

FIGURE 5. Wake parameter compared with Coles data fit. ●, Coles constants: $\kappa = 0.41$ and $B = 5.0$; ○, Zagarola constants: $\kappa = 0.436$ and $B = 6.13$; ◇, Osterlund constants: $\kappa = 0.38$ and $B = 4.1$.

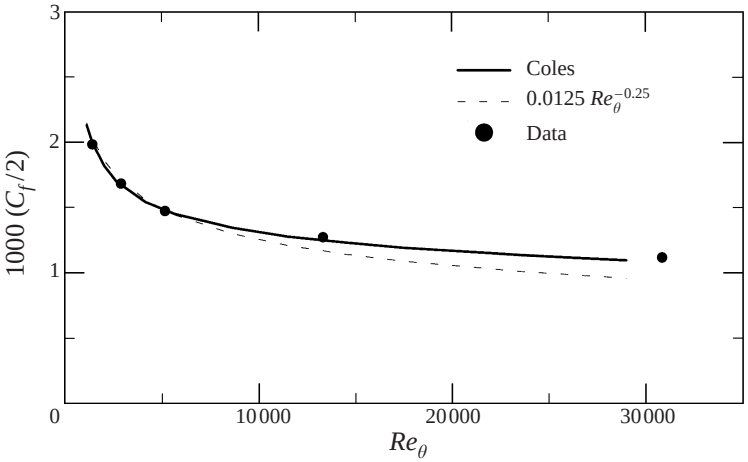

FIGURE 6. C_f compared with Coles data fit.

Figure 6 shows the variation of C_f with Re_θ, compared with the empirical fit of Coles (1962), and the $\frac{1}{7}$th power law correlation. The data indicate that the exponent in the power law is a decreasing function of Re_θ, and that C_f estimates based on the $\frac{1}{7}$th power law are only accurate at low Reynolds number.

3.2. *Streamwise normal stress*

It is generally assumed *a priori* that if the mean flow near the wall scales on inner coordinates, then so too must the Reynolds stresses, which rely on the mean gradients for their energy (Townsend 1956; Tennekes & Lumley 1972):

$$\overline{u'^2}/u_\tau^2 = F_4(y^+), \tag{3.11}$$

$$\overline{v'^2}/u_\tau^2 = F_5(y^+), \tag{3.12}$$

$$\overline{u'v'}/u_\tau^2 = F_6(y^+). \tag{3.13}$$

Thus, the Reynolds stresses are almost always normalized by inner scales, u_τ, and ν/u_τ (indicated by a '+' superscript). Unfortunately, the collapse of the Reynolds stresses in inner scaling is generally not supported by measurements.

Profiles of $\overline{u'^2}^+$ which resolve the near-wall behaviour show a peak very near the wall. The magnitude and location of this peak as a function of Reynolds number is still in doubt. Klewicki, Murray & Falco (1994) found an empirical fit for the peak magnitude of the stream-wise normal stress:

$$\overline{u'^2}^+_{max} = 8.5 \times 10^{-9}\, Re_\theta^2 + 4.8 \times 10^{-4}\, Re_\theta + 6.86. \tag{3.14}$$

By plotting data from 18 different experiments (16 hot-wire and 2 LDA) from $Re_\theta = 300$ to $Re_\theta = 20\,000$, Mochizuki & Nieuwstadt (1996) conclude that the peak value is essentially constant:

$$\overline{u'^2}^+_{max} = 7.34. \tag{3.15}$$

They also found that the location of the peak follows the trend:

$$y^+(\overline{u'^2}^+_{max}) = 1.7 \times 10^{-4}\, Re_\theta + 14.4. \tag{3.16}$$

The flat-plate data from Purtell, Klebanoff & Buckley (1981) show an increasing peak value of $\overline{u'^2}^+$ up to $Re_\theta = 1340$, followed by a slowly decreasing peak for Reynolds numbers up to 5100. Andreopoulos *et al.* (1984) show a steady decline with increasing Reynolds number for Re_θ from 3600 to 15 400. A thorough review by Gad-el-Hak & Bandyopadhyay (1994) concludes that there is no definite trend except perhaps an initial rise, and then a slow drop of the peak value of $\overline{u'^2}^+$. They further conclude that 'the data ... indicate that the turbulence intensity profiles do not collapse even deep into the inner layer.' Sreenivasan (1989) shows data from ten experiments over a wide Reynolds-number range, and concludes the y^+ location of the peak $\overline{u'^2}^+$ is 'sensibly independent of Reynolds number.'

Still more data are summarized by Fernholz & Finley (1996), who state that there is a weak Reynolds-number dependence in the peak value of $\overline{u'^2}^+$, as well as a possible rise in the location of the peak $\overline{u'^2}^+$ from $y^+ = 12$ to $y^+ = 16$ with increasing Reynolds number. Further from the wall, all of the profiles show a consistent increase in the magnitude of $\overline{u'^2}^+$ with Reynolds number. In fact, some of the highest-Reynolds-number cases show a second maximum in the $\overline{u'^2}^+$ profiles at $y^+ \approx 400$) (Bruns, Dengel & Fernholz 1992; Fernholz *et al.* 1995).

Marusic, Uddin & Perry (1997) have proposed a universal curve for $\overline{u'^2}^+$ in terms of y/δ and y^+ for the region $y^+ > 100$ based on the attached eddy hypothesis of Townsend (1976). Their formulation includes a logarithmic region in the inner layer, with a viscous deviation near the wall, a wake deviation in the outer region, and switching functions to turn these deviations on and off. Their formulation predicts that $\overline{u'^2}^+$ in the inner region will rise without limit for a fixed y^+ as the Reynolds number increases. This is consistent with the scaling which will be presented here (assuming that C_f goes to zero as Re_θ goes to infinity). Their formulation, however, predicts this rise to be logarithmic, while the scaling used here, $C_f^{-0.5}$, goes to infinity much more slowly (as evidenced by the over-prediction of C_f by the $\frac{1}{7}$th power law at high Reynolds number in figure 6).

Figure 7 shows $\overline{u'^2}$ in inner coordinates, and clearly demonstrates that the magnitude of $\overline{u'^2}^+$ is a strong function of Reynolds number throughout the entire inner region

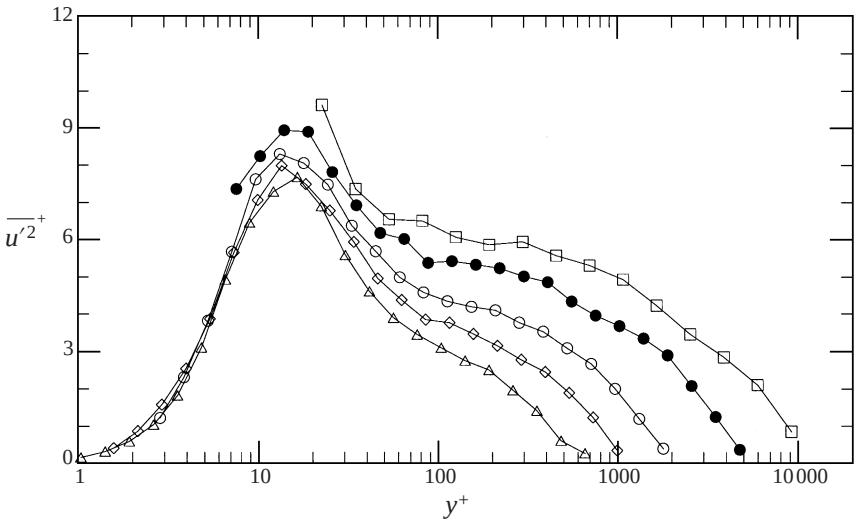

FIGURE 7. $\overline{u'^2}$ in inner–inner coordinates. Symbols in table 1.

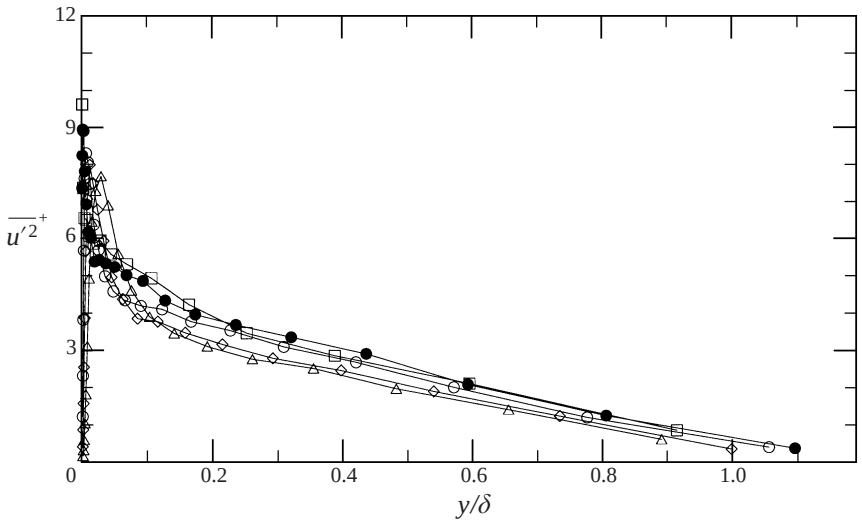

FIGURE 8. $\overline{u'^2}$ in inner–outer coordinates. Symbols in table 1.

except the sublayer. The near-wall peak occurs at $y^+ = 14$, and grows in magnitude with increasing Reynolds number. Figure 8 shows $\overline{u'^2}^+$ plotted against y/δ. The increasing value of $\overline{u'^2}$ in the outer region with Reynolds number is again evident.

Note that we have elected to use δ as the outer lengthscale for all of the turbulence quantities because it is more independent of the velocity profile shape than the integral parameters. Many researchers prefer to use integral lengthscales because of a perceived large uncertainty in measuring δ. Since δ depends only on the velocity magnitudes relative to each other, however, systematic uncertainty in the velocity measurement does not contribute to uncertainty in δ. Provided that the flow facility is steady, only statistical uncertainty of the mean velocity measurements contributes to uncertainty in δ. This can be calculated with a perturbation analysis (Moffat 1988),

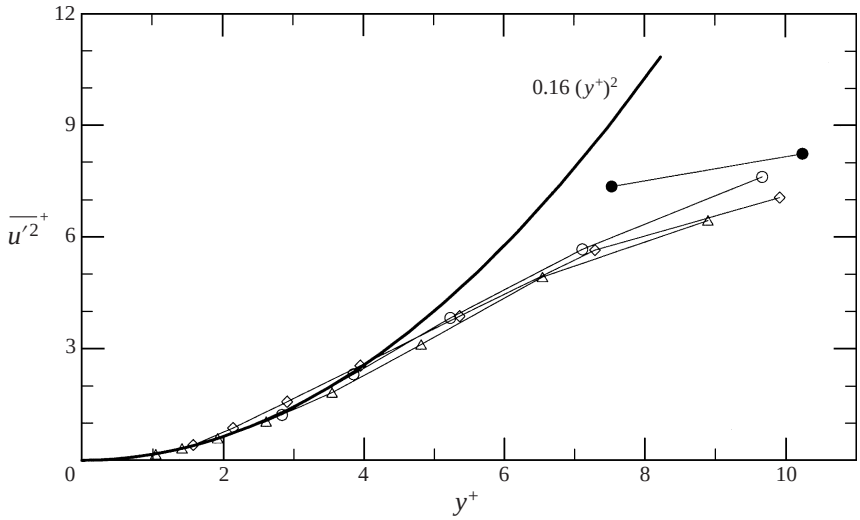

FIGURE 9. Sublayer behaviour of $\overline{u'^2}$. Symbols in table 1.

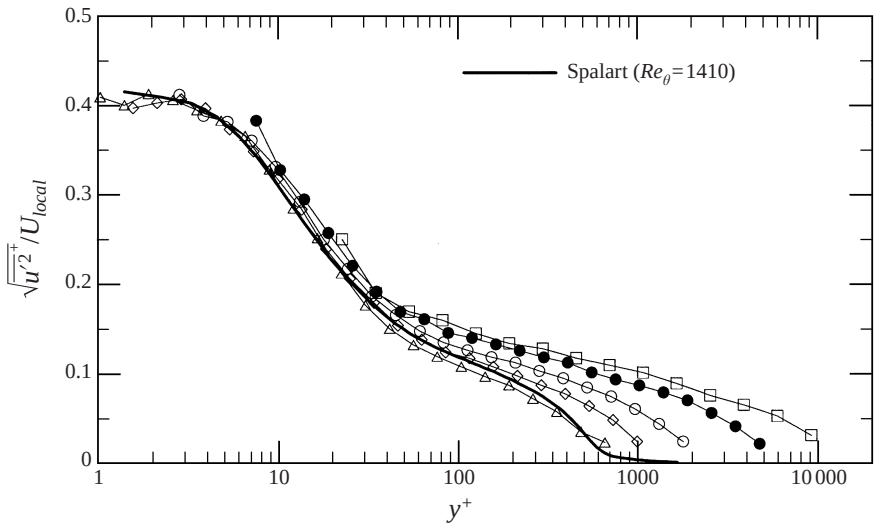

FIGURE 10. Ratio of the r.m.s. streamwise velocity to local mean velocity. Symbols in table 1.

which estimates the uncertainty in δ for the $Re_\theta = 31\,000$ case to be $\pm 3\%$, and for the lower-Reynolds-number cases, $\pm 1\%$.

A close up of the normal stress in the sublayer is shown in figure 9. Also shown in the plot is the first term of the Taylor series expansion of $\overline{u'^2}^+$ around $y = 0$ (Monin & Yaglom 1971):

$$\overline{u'^2}^+ = A_1(y^+)^2 + \cdots. \tag{3.17}$$

When evaluating the constant, we should keep in mind that the uncertainty in the sublayer velocity measurements is large. The best-fit value of A_1 is approximately 0.16, and (3.17) is accurate for $y^+ < 4$.

The ratio of $\sqrt{\overline{u'^2}}$ to the streamwise mean velocity at each point is shown in figure 10, compared with the calculation of Spalart (1988). This ratio is poorly behaved near

the wall since both $\overline{u'^2}$ and U go to zero. The agreement of the data with the calculation at the wall provides a stringent check on the accuracy of the near-wall measurements. The profiles which extend below $y^+ \approx 3$ show the limiting value of $\sqrt{\overline{u'^2}}/U$ at the wall is approximately 0.41 ($1430 < Re_\theta < 5200$). This value is also confirmed by the direct numerical simulation of Antonia & Kim (1994), and the hot-wire measurements of Alfredsson *et al.* (1988). Note that in the sublayer, where $U^+ = y^+$, this limiting value can be estimated using the near-wall expression $\overline{u'^2}^+ = 0.16(y^+)^2$ shown in figure 9. This predicts that the sublayer value of $\sqrt{\overline{u'^2}}/U_{local} = 0.40$, which agrees within the uncertainty of the measurement.

The increasing trend in $\sqrt{\overline{u'^2}}/U$ with Reynolds number for $y^+ > 6$ further confirms that $\overline{u'^2}$ scales differently from the mean velocity.

3.2.1. *Hot-wire spatial resolution*

While the increase in $\overline{u'^2}^+$ in the outer region has been observed by many workers, the steady increase of the near-wall peak ($y^+ = 14$) with increasing Reynolds number is contrary to the conclusion of many hot-wire experiments which find an essentially constant near-wall peak (Mochizuki & Nieuwstadt 1996), or a peak which initially increases, and then decreases with increasing Reynolds number (Gad-el-Hak & Bandyopadhyay 1994). It is well known that there is a strong effect of hot-wire length (non-dimensionalized by ν/u_τ) on the measured value of $\overline{u'^2}$ (Sreenivasan 1989; Klewicki *et al.* 1994; Fernholz & Finley 1996). Since a hot wire measures the average heat transfer rate over its length, it will attenuate the measured velocity fluctuation if that fluctuation occurs over a lengthscale smaller than the length of the hot wire. The question then becomes: what fraction of the turbulent kinetic energy is carried by eddies smaller than the wire length? The attenuation of $\overline{u'^2}$ will be proportional to the fraction of energy carried by these small eddies. If the characteristic eddy size is taken to be the distance to the wall (Tennekes & Lumley 1972), and it is assumed that a non-negligible fraction of the turbulent kinetic energy is carried by eddies with size of the order of the distance to the wall, then a hot wire will significantly attenuate the measured turbulence when it is positioned closer to the wall than its length, i.e. $y^+ < l^+$. When taken with the requirement that l/d of a hot wire must be greater than 200 to avoid conduction errors, the hot wire becomes rather limited: in order for a 2.5 μm diameter hot wire to measure accurately the near-wall peak in $\overline{u'^2}$ at $y^+ = 14$, the viscous lengthscale, ν/u_τ, must be larger than approximately 36 μm. This corresponds to a low Reynolds number unless the flow facility is extremely large.

One of the most stringent tests for resolution errors is the previously discussed ratio: $\sqrt{\overline{u'^2}}/U$. The LDA results for $Re_\theta = 1430$ and $Re_\theta = 13\,000$ are compared to hot-wire measurements in figure 11. The hot-wire data were taken with a constant-temperature 2.5 μm diameter hot wire (overheat ratio of 1.8). The active length of the wire was 600 μm, which gives $l^+ = 10$ for the $Re_\theta = 1430$ case, and $l^+ = 75$ for the $Re_\theta = 13\,000$ case. Consistent with the scaling argument that l^+ should be of the same order or greater than y^+ to obtain accurate $\overline{u'^2}$, the hot-wire measurements of $\overline{u'^2}$ become increasingly attenuated below approximately $y^+ \approx 8$ for the low-Reynolds-number case, and $y^+ \approx 80$ for the higher Reynolds number.

This hot-wire size limitation is confirmed by Alfredsson *et al.* (1988), who conclude that hot wires need $l^+ < 6$ to measure $\sqrt{\overline{u'^2}}/U = 0.4$ very near the wall. Somewhat less stringent guidelines for maximum l^+ are given by Ligrani & Bradshaw (1987). By measuring the maximum of the near-wall peak in $\overline{u'^2}$ with increasingly small wire

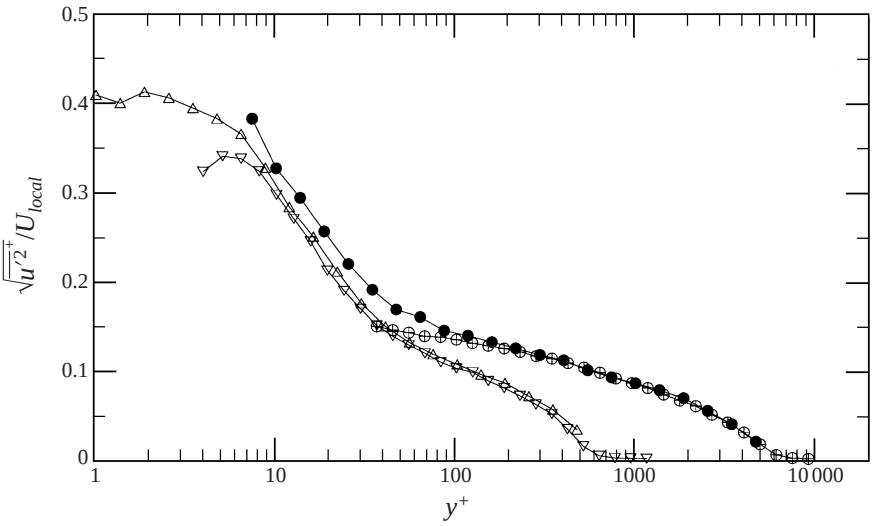

FIGURE 11. Comparison of LDA and hot-wire: ratio of r.m.s. streamwise velocity to local mean velocity. At $Re_\theta = 13\,000$: ●, LDA; ⊕, hot wire. At $Re_\theta = 1430$: △, LDA; ▽, hot wire.

length, they recommend $l^+ < 20 - 25$ for resolving the near-wall turbulence. This result is supported by Khoo, Chew & Li (1997), who conclude that $l^+ < 22$ resolves $\overline{u'^2}$ for $y^+ > 5$. Johansson & Alfredsson (1983) report a 10% decrease in the near-wall peak of $\overline{u'^2}$ in comparing results of a wire with $l^+ = 32$ to those of a wire with $l^+ = 16$.

It should be noted that it is only useful to quote a maximum allowable wire length in viscous units if a minimum allowable wall height is also quoted in viscous units, because l/y is the essential parameter. The data presented here indicate that Ligrani & Bradshaw (1987) and Khoo, Chew & Li (1997) are rather optimistic, and that the commonly measured trend of an increasing $\overline{u'^2}$ peak at low Reynolds number, followed by a decrease at high Reynolds number, is consistent with a well-resolved $\overline{u'^2}$ measurement at low Reynolds numbers, followed by a gradual loss of spatial resolution with increasing Reynolds number.

3.2.2. *A new scaling for* $\overline{u'^2}$

The Reynolds-number dependence of $\overline{u'^2}$ contradicts (3.11). To resolve this inconsistency, Townsend (1961) proposed that the turbulent motion in the near-wall region consists of the superposition of 'active' and 'inactive' motions. The active motions produce the shear stress, and scale on inner variables. The inactive motion is a 'meandering or swirling motion made up from attached eddies of large size which contribute to the Reynolds stress much further from the wall than the point of observation.' The contribution to $\overline{u'^2}$ from the inactive motions presumably scales on y/δ, which results in the Reynolds-number dependence of $\overline{u'^2}$ (Bradshaw 1967).

The failure of $\overline{u'^2}^+$ to collapse has led researchers to experiment with a variety of inner–outer mixed scalings. Perry & Li (1990) use a mixed lengthscale which is proportional to $\delta^*\sqrt{2/C_f}$ to plot $\overline{u'^2}$ data. George & Castillo (1997) conclude from asymptotic analysis of the Navier–Stokes equations that the proper velocity scale for $\overline{u'^2}$ is U_e^2. Fernholz & Finley (1996) use the Rotta (1962) lengthscale $\Delta = y/\delta^*\sqrt{C_f/2}$ to plot turbulence quantities.

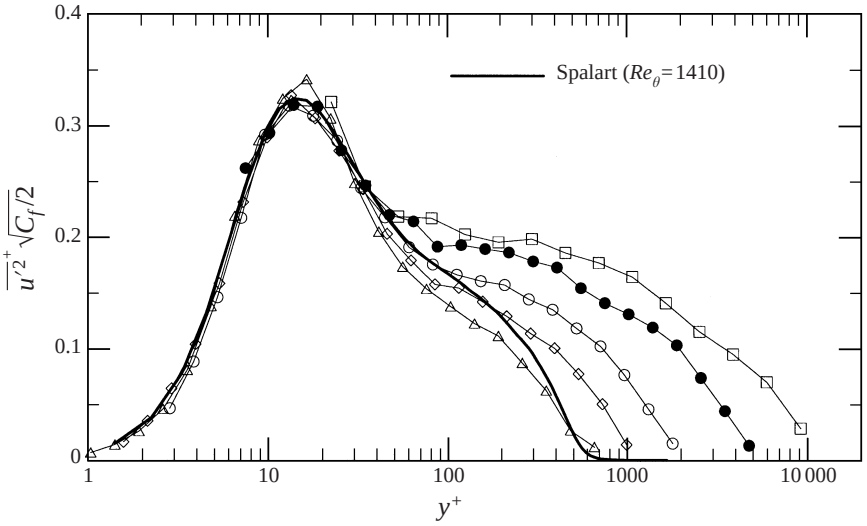

FIGURE 12. $\overline{u'^2}^+\sqrt{C_f/2}$ in mixed–inner coordinates. Symbols in table 1.

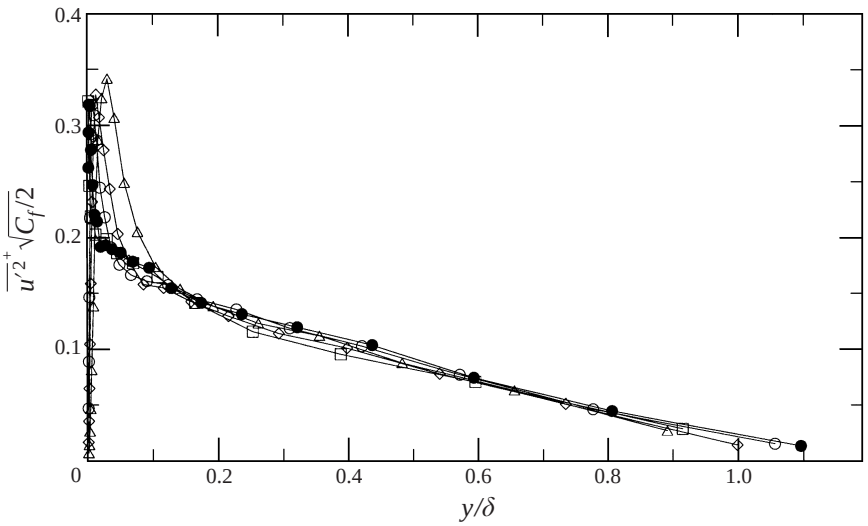

FIGURE 13. $\overline{u'^2}^+\sqrt{C_f/2}$ in mixed–outer coordinates. Symbols in table 1.

The observation that the peak magnitude of $\overline{u'^2}^+$ changes roughly proportionally to $Re_\theta^{0.1}$ led us to use a mixed inner and outer velocity scaling for $\overline{u'^2}$. Figure 12 is a plot of $\overline{u'^2}^+\sqrt{C_f/2}$, (or equivalently $\overline{u'^2}/u_\tau U_e$), vs. y^+, which shows remarkably good collapse of the near-wall peak at $y^+ = 14$ out to $y^+ \approx 60$. The same scaling vs. y/δ is shown in figure 13, and shows good collapse of the data in the outer region. This scaling will be denoted by $\overline{u'^2}^\circ$.

Classical arguments do not support any scaling other than u_τ^2 for the inner region, but there is a vast quantity of data which demonstrates that this velocity scaling does not have any universal behaviour, particularly in the log region and outer region. A possible justification for a mixed velocity scaling comes from the energy balance of the boundary layer. The total power dissipated by the boundary layer scales on

$U_e\tau_w$, which, for constant density flow, is proportional to $U_e u_\tau^2$. Thus, the total rate of energy dissipation by the turbulence depends on both U_e and u_τ.

Using the boundary layer approximations, the rate of energy transfer from the outer part of the boundary layer to the inner region can be expressed as (Rotta 1962)

$$\frac{1}{\rho}\frac{\mathrm{d}(\tau_w U)}{\mathrm{d}y} = -\overline{u'v'}\frac{\mathrm{d}U}{\mathrm{d}y} + \nu\left(\frac{\mathrm{d}U}{\mathrm{d}y}\right)^2, \tag{3.18}$$

indicating that the energy is lost to the turbulence through $-\overline{u'v'}(\mathrm{d}U/\mathrm{d}y)$, and to direct dissipation by the mean velocity gradient. The energy lost to the turbulence appears as the turbulent kinetic energy production term in the transport equation for $\overline{u'^2}$, showing that the energy from the mean flow is first transferred to $\overline{u'^2}$, and then redistributed by pressure and turbulent transport to the other Reynolds stresses. Since the rate at which energy is dissipated by the boundary layer is proportional to $U_e u_\tau^2$, it is plausible that the magnitude of $\overline{u'^2}$ depends on both u_τ and U_e. It is difficult to say, however, why it would scale on the product of U_e and u_τ. It is possible that the behaviour of $\sqrt{C_f/2}$ is merely fortuitous, and is actually masking other Reynolds-number effects which are genuinely responsible for the observed behaviour. The collapse of the $\overline{u'^2}^\circ$ profiles over this wide range of Reynolds number, however, is convincing empirical evidence of the effectiveness of this scaling in defining self-similar profiles for $\overline{u'^2}$. Since the 'active' motions should scale on u_τ^2, the success of this mixed scaling indicates that the fraction of turbulent kinetic energy carried by 'inactive' motions is approximately u_τ/U_e (or $\sqrt{C_f/2}$), the ratio of inner to outer velocity scales.

A study by Osterlund (1999) measured $\overline{u'^2}$ with hot wires in a facility large enough to maintain $l^+ < 10$ for Re_θ up to 10 000. He found that the near-wall peak in $\overline{u'^2}^+$ increases with Reynolds number. Replotting these data in $\overline{u'^2}^\circ$ coordinates, the peaks collapse to 0.30, with no apparent Reynolds-number trend. While this is slightly below the 0.32 peak measured here, the combined uncertainties of the experiments overlap, which supports the universality of this scaling. Since this result has profound implications for turbulence modelling, it is imperative that it be corroborated by other high-Reynolds-number experiments with high enough spatial resolution to accurately resolve the Reynolds stresses.

3.3. *Wall-normal normal stress*

Measurements of the near-wall variation of $\overline{v'^2}$ with Reynolds-number are very rare. Almost all the data are from experiments which used cross-wires, which cannot come nearly as close to the wall as a single-wire probe, and even magnitudes measured in the outer region with different probes are not in good agreement. Fernholz & Finley (1996) show cross-wire measurements compiled from Andreopoulos *et al.* (1984), Roach & Brierley (1989), Erm & Joubert (1991), Bruns *et al.* (1992), and Fernholz *et al.* (1995), which suggest the location of the maximum $\overline{v'^2}^+$ follows

$$y^+(\overline{v'^2}^+_{max}) = 0.071\ Re_\theta, \tag{3.19}$$

for $2500 < Re_\theta < 58\,000$. The data also show a general increase in the magnitude of $\overline{v'^2}^+$ with increasing Reynolds number, although the scatter is quite large.

Sreenivasan (1989) plots the peak location from 12 different hot-wire data sets, and finds that the peak location of the maximum $\overline{v'^2}^+$ is also a strong function of

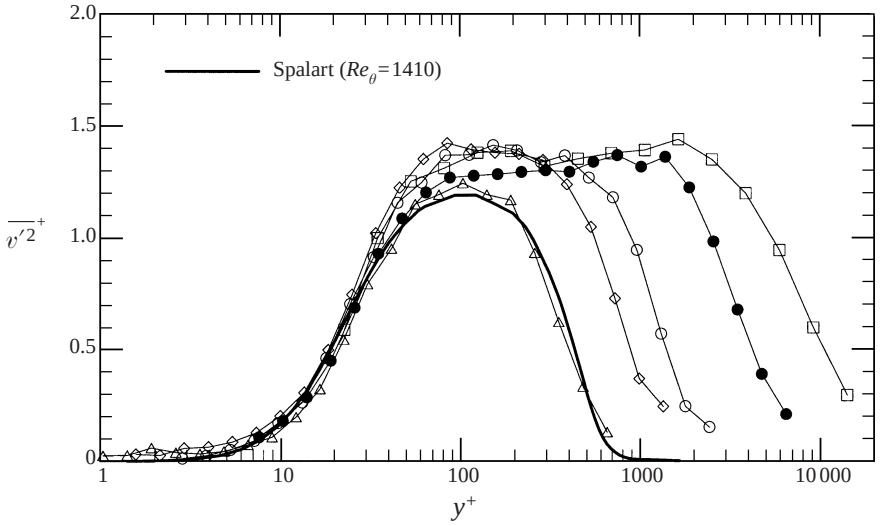

FIGURE 14. $\overline{v'^2}$ in inner–inner coordinates. Symbols in table 1.

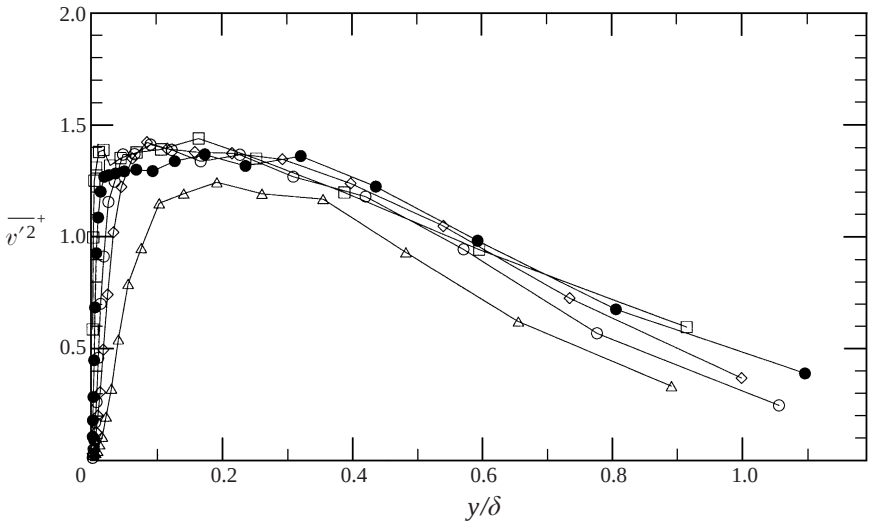

FIGURE 15. $\overline{v'^2}$ in inner–outer coordinates. Symbols in table 1.

Reynolds number. He defines a rough fit to the data:

$$y^+(\overline{v'^2}^+_{max}) = (Re_\delta \sqrt{C_f/2})^{0.75}. \tag{3.20}$$

Figure 14 shows the present $\overline{v'^2}$ measurements in inner coordinates, and figure 15 shows the same data plotted vs. y/δ. Although there is some scatter, no Reynolds-number trend is evident in the collapse of the profiles in inner coordinates from the wall to the end of the log region. A plateau of $\overline{v'^2}^+ \approx 1.35$ extends from $y^+ = 100$ to $y/\delta \approx 0.25$. The exception is the lowest-Reynolds-number case, which is evidently showing low-Reynolds-number effects. The data show good agreement with the calculation of Spalart (1988), indicating the accuracy of the measurements at low

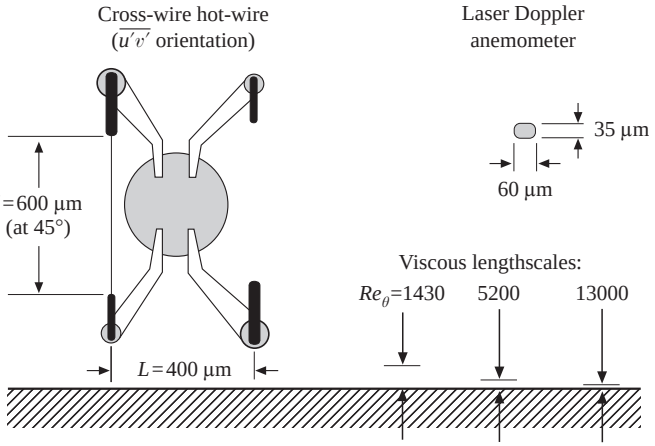

FIGURE 16. Comparison of cross-wire hot-wire and LDA measurement volume sizes.

Reynolds number. The drop in $\overline{v'^2}^+$ is fairly linear in y/δ for $y/\delta > 0.25$, although the data are too scattered to make any firm conclusions.

The universality of $\overline{v'^2}^+$ in the inner region is consistent with the scaling arguments used to derive the law of the wall. To attain self-similar profiles in the outer region, the correct lengthscale is δ, as shown by Townsend (1956). This results in the different length scales for the inner and outer region:

$$\overline{v'^2}^+_{inner\ region} = f(y^+), \tag{3.21}$$

$$\overline{v'^2}^+_{outer\ region} = f(y/\delta). \tag{3.22}$$

In general, since the ratio of these lengthscales is always a function of Reynolds number, a Reynolds-number-dependent matching function is required to connect the inner and outer regions. No matching function is necessary, however, if both functions go to a constant, e.g. 1.35, although the location of the overlap may still be a function of Reynolds number. These data indicate that $\overline{v'^2}$ shows reasonable self-similarity over the entire boundary layer.

Since the magnitude of $\overline{v'^2}$ scales on u_τ^2, the transfer rate of turbulent energy from $\overline{u'^2}$ to $\overline{v'^2}$ must scale on inner coordinates, despite the fact that the magnitude of $\overline{u'^2}$ does not scale on u_τ^2.

Figure 16 is a scale drawing for comparing the relative sizes of the cross-wire and the LDA measurement volume, with the viscous lengthscales at different Reynolds numbers. The cross-wire probe is shown in an end-on view, positioned to measure $\overline{u'v'}$ and $\overline{v'^2}$. It has an etched active length of 600 μm, and a wire spacing of 400 μm, making it smaller than commercially available cross-wire probes. A comparison of the cross-wire size with the viscous lengthscales indicates that spatial resolution is a significant problem for cross-wires even at low Reynolds numbers. As figure 16 shows, the active lengths of the wire are positioned across the mean velocity and Reynolds stress gradients. This makes it difficult to define where the measurement is being made, because the hot wire is a highly nonlinear device.

The most serious problem with a cross-wire, however, is that it combines the velocity component normal to one wire with the velocity component normal to the other wire, in order to resolve the two velocity components at the point between the wires. Extrapolating the wire-normal velocity components to the centre point between

the two wires gives

$$V_{c,1} = V_1 + \frac{L}{2}\frac{\partial V_1}{\partial z} + \cdots, \tag{3.23}$$

$$V_{c,2} = V_2 - \frac{L}{2}\frac{\partial V_2}{\partial z} + \cdots, \tag{3.24}$$

where $V_{c,1}$ is the velocity component perpendicular to wire 1 extrapolated to the point in the centre of the wires, V_1 is the measured velocity component perpendicular to wire 1 at wire 1, and correspondingly for wire 2. Note that the use of L for the distance is rather optimistic, since it is actually the smallest distance between the wires. For an ideal cross-wire with wires at $\pm 45^\circ$, the velocity components are resolved into tunnel coordinates:

$$u = \frac{1}{\sqrt{2}}(V_{c,1} + V_{c,2}) = \frac{1}{\sqrt{2}}(V_1 + V_2) + \frac{L}{2\sqrt{2}}\left(\frac{\partial V_1}{\partial x} - \frac{\partial V_2}{\partial x}\right) + \cdots, \tag{3.25}$$

$$v = \frac{1}{\sqrt{2}}(V_{c,1} - V_{c,2}) = \frac{1}{\sqrt{2}}(V_1 - V_2) + \frac{L}{2\sqrt{2}}\left(\frac{\partial V_1}{\partial x} + \frac{\partial V_2}{\partial x}\right) + \cdots. \tag{3.26}$$

The first error term is of order L, indicating that an instantaneous spanwise velocity gradient between the two wires contributes to the error in measurement of both u and v. While this is not a substantial problem for the u-component, since V_1 and V_2 are both large, the error term can be very large for the v-component, since V_1 and V_2 are very nearly the same size. The problem arises because the measured velocity component at each wire is

$$V = \left\{ w^2 + \left(\frac{u}{\sqrt{2}} \pm \frac{v}{\sqrt{2}} \right)^2 \right\}^{0.5}, \tag{3.27}$$

so any difference between the wires in u or in w will be interpreted as v. Most unsettling is equation (3.26), which shows that even if the spanwise gradient at the two wires is the same, i.e. a turbulent eddy which is larger than the wire spacing, there is a contribution from the first-order error term. Thus, a cross-wire will erroneously measure $\overline{v'^2}$ from any eddy which cools one wire more than the other, whether the eddy is small enough to pass over only one wire, or large enough to create a spanwise gradient across both wires. These effects will cause $\overline{v'^2}$ to be overestimated by a cross-wire (Moin & Spalart 1987; Park & Wallace 1993), and are consistent with the tendency of cross-wires to show an increasing value of $\overline{v'^2}^+$ with increasing Reynolds number.

3.4. *Reynolds shear stress*

The measurement of $\overline{u'v'}$ with a cross-wire is also problematic, as evidenced by the many data sets which fail to show $-\overline{u'v'}$ approaching u_τ^2 near the wall. This quantity also is difficult to measure accurately with standard laser Doppler velocimetry, because the results are usually somewhat dependent on the chosen coincidence time interval, which determines whether a u-component measurement and a v-component measurement came from the same particle. The present LDA system, however, obtains both u-component and v-component information from each burst, and therefore does not have any dependence on coincidence (see DeGraaff & Eaton (1999) for further details).

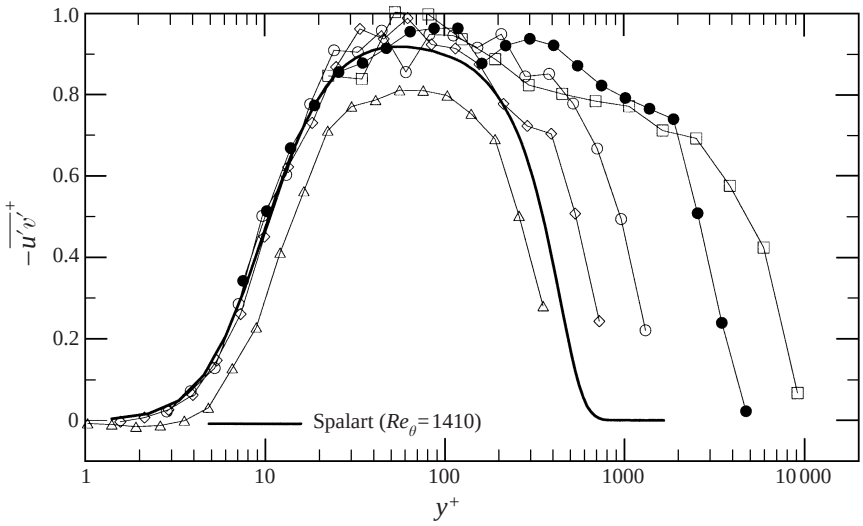

FIGURE 17. $\overline{u'v'}$ in inner–inner coordinates. Symbols in table 1.

Sreenivasan (1989) plots the y^+ location of the peak in $\overline{u'v'}^+$, and fits the correlation:

$$y^+(\overline{u'v'}^+_{max}) = 2\ (Re_\delta \sqrt{C_f/2})^{0.5}. \tag{3.28}$$

Fernholz & Finley (1996) do not assume *a priori* that the correct maximum for $\overline{u'v'}^+$ is unity, and conclude from the data of Klebanoff (1955), Bruns *et al.* (1992), Klewicki *et al.* (1994), and Fernholz *et al.* (1995), that despite rather large scatter, there is no Reynolds-number dependence of the peak magnitude of $\overline{u'v'}^+$. Their plot indicates the peak value is between 0.8 and 1.0, and they find that the peak location is a function of Reynolds number:

$$y^+(\overline{u'v'}^+_{max}) = {Re_\theta}^{0.61}. \tag{3.29}$$

Because the total shear stress consists of the Reynolds stress and the viscous shear stress, we can conclude several things *a priori*. First, since the velocity gradient at the wall must scale the velocity gradient near the wall, and since the total shear stress near the wall cannot change rapidly in the wall-normal direction for a slowly growing boundary layer, $\overline{u'v'}$ must scale on u_τ^2 near the wall (equation (3.13)). Secondly, in a flat-plate boundary layer, the maximum total shear stress, $\overline{u'v'} + \nu(\mathrm{d}U/\mathrm{d}y)$, occurs at the wall. These two statements imply that the peak in the Reynolds stress must be near the wall, the peak location must scale on y^+, and it must have a magnitude less than but nearly equal to u_τ^2.

The Reynolds shear stress is shown in figure 17 vs. y^+, and in figure 18 vs. y/δ. The behaviour is similar to $\overline{v'^2}$, although the data are somewhat more scattered. The magnitude of $\overline{u'v'}^+$ reaches a peak of approximately 0.95 at $y^+ \approx 70$. The outer layer again shows an approximately linear decrease with y/δ. In contrast to $\overline{v'^2}$, $\overline{u'v'}$ does not show an extended plateau of constant magnitude. Note that the magnitudes of the slightly non-negative values of $\overline{u'v'}$ very near the wall for the lowest-Reynolds-number case are less than the near-wall uncertainty, and should be zero.

The lowest-Reynolds-number case does not agree well with the calculation of Spalart (1988), however, the LDA does consistently measure the total shear stress equal to the wall shear stress throughout the near-wall region for the other Reynolds-

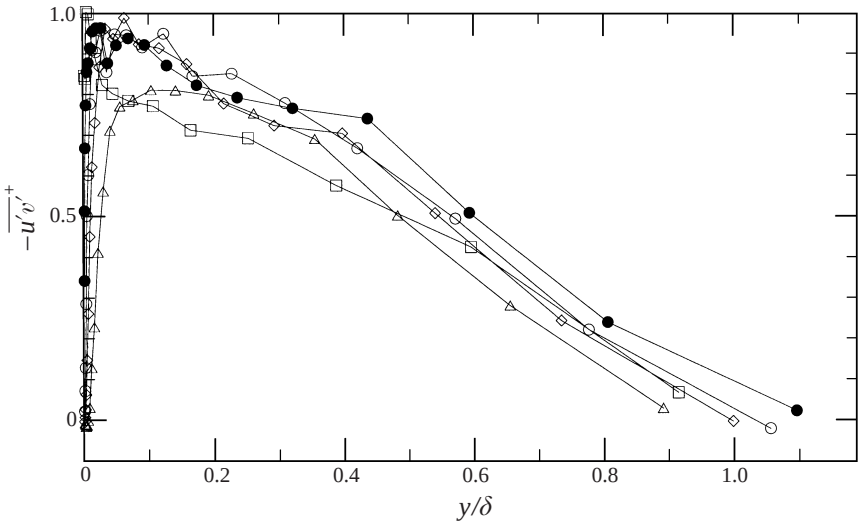

FIGURE 18. $\overline{u'v'}$ in inner–outer coordinates. Symbols in table 1.

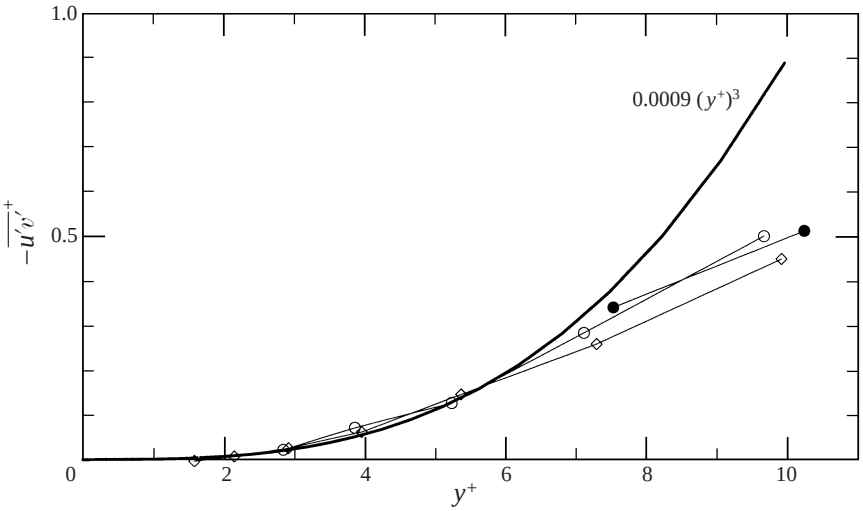

FIGURE 19. Sublayer behaviour of $\overline{u'v'}$. Symbols in table 1.

number cases (which will be shown in figures 20 to 24). It therefore seems likely that the $\overline{u'v'}$ peak is accurately measured for this boundary layer, suggesting that either the boundary layer for this low Reynolds-number is not 'canonical', i.e. the slight favourable pressure gradient has depressed the $\overline{u'v'}$ peak, or that the calculation has over-predicted $\overline{u'v'}$.

Figure 19 shows the sublayer behaviour $\overline{u'v'}$. The first term of the Taylor series expansion of $\overline{u'v'}$ around $y = 0$ is (Monin & Yaglom 1971)

$$\overline{u'v'} = A_2(y^+)^3 + \cdots. \tag{3.30}$$

Fitting the experimental data yields $A_2 = 0.0009$, which is fairly accurate for $y^+ < 6$.

The total shear stress is the sum of the viscous shear stress and the Reynolds shear stress. These three quantities are plotted in figures 20 to 24 for each Reynolds

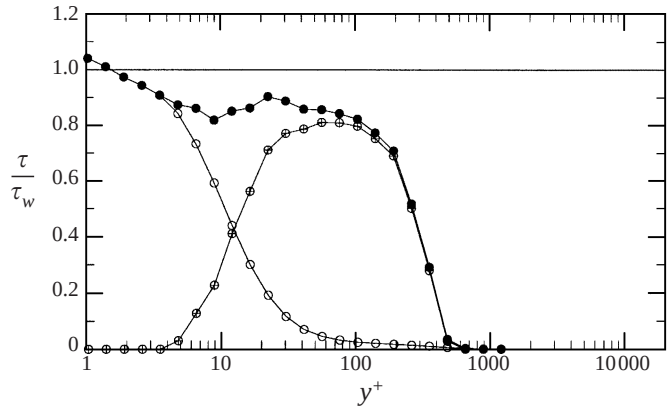

FIGURE 20. Shear stress distribution for $Re_\theta = 1430$: ●, total shear; ⊕, Reynolds shear; ○, viscous shear.

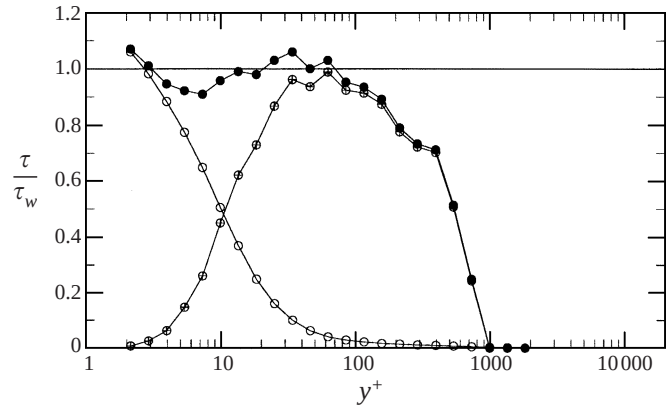

FIGURE 21. Shear stress distribution for $Re_\theta = 2900$. Symbols as in figure 20.

number. It should be noted that there is additional uncertainty in computing the viscous shear, particularly for the closely spaced data points near the wall, since the data must be differentiated.

With the exception of the lowest-Reynolds-number case (figure 20), the total stress is approximately equal to the wall stress over a substantial region extending from the wall (figures 21 to 24). The viscous stress profiles show a small contribution to the total shear from viscosity even above $y^+ = 100$. For figures 21 to 23, the viscous shear and Reynolds stress cross at $y^+ \approx 10$, and $\tau/\tau_w \approx 0.5$. This result provides strong evidence for the universality of the near-wall region. For the lowest-Reynolds-number case, the total shear stress drops below u_τ^2 much closer to the wall, and the viscous stress contribution extends further from the wall. These are presumably low-Reynolds-number effects, i.e. the viscosity is important through a substantial fraction of the inner region, so the boundary layer has not yet achieved self-similarity. The point where the viscous shear and the Reynolds shear are equal is the position of maximum turbulent energy production (Rotta 1962).

Figure 25 shows the total stresses from figures 20 to 24 plotted vs. y/δ. The linearly decreasing total shear stress profile of a channel flow is shown for comparison. The y/δ axis scale is logarithmic to emphasize that the assumption of a 'nearly constant

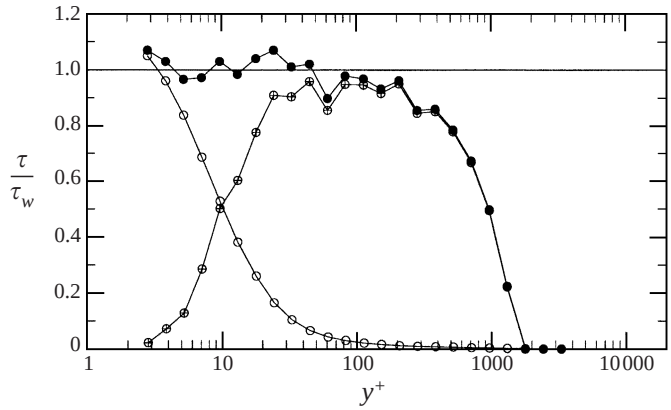

FIGURE 22. Shear stress distribution for $Re_\theta = 5200$. Symbols as in figure 20.

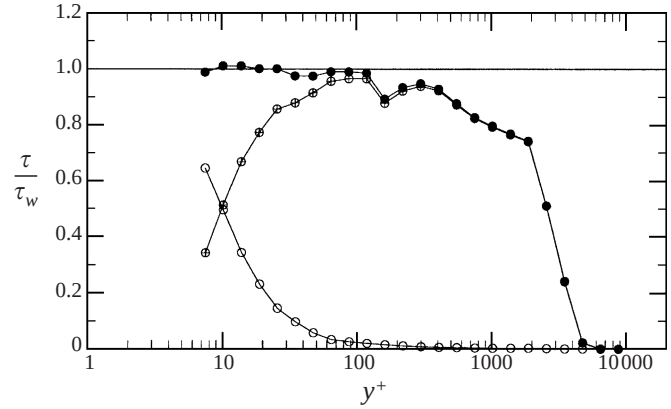

FIGURE 23. Shear stress distribution for $Re_\theta = 13\,000$. Symbols as in figure 20.

stress region' near the wall is not inconsistent with a linearly decreasing total stress profile. As figure 17 shows, however, these data are too scattered to firmly determine the total shear stress profile shape for an equilibrium boundary layer.

3.5. *Reynolds stress production*

There are very few boundary-layer data which show the near-wall peaks of the turbulent kinetic energy production or Reynolds shear stress production. In their review, Gad-el-Hak & Bandyopadhyay (1994) report (without showing data) that the peak production of turbulent kinetic energy occurs at $y^+ \approx 15$, independent of Reynolds number.

The production of turbulent kinetic energy is shown in figure 26. The data collapse well in inner coordinates, with the exception of the lowest-Reynolds-number case, which shows a depressed near-wall peak. It is clear again that the lowest-Reynolds-number case is influenced by low-Reynolds-number effects.

Differentiating equation (3.18) with respect to $\mathrm{d}U/\mathrm{d}y$ shows that the maximum production occurs where

$$-\overline{u'v'} = \nu\left(\frac{\mathrm{d}U}{\mathrm{d}y}\right) = \frac{u_\tau^2}{2}, \tag{3.31}$$

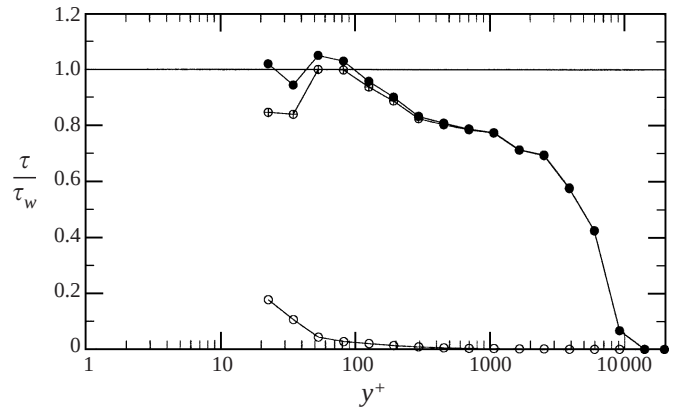

FIGURE 24. Shear stress distribution for $Re_\theta = 31\,000$. Symbols as in figure 20.

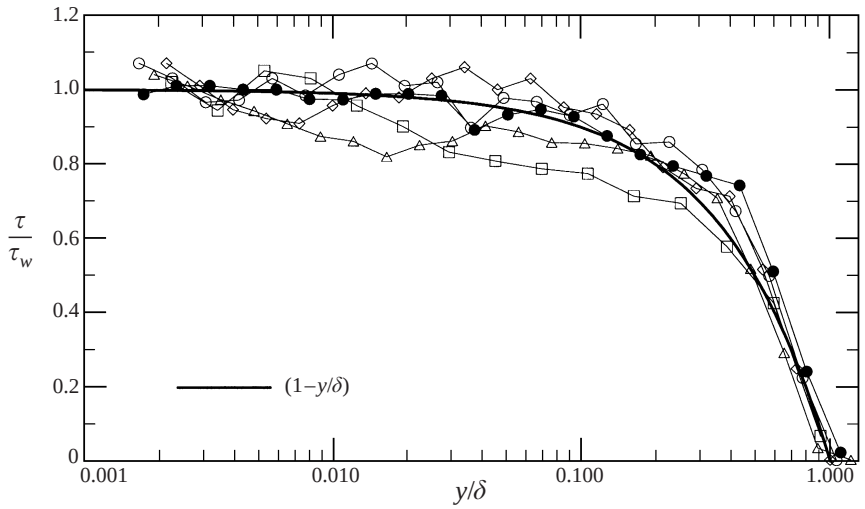

FIGURE 25. Total shear stress distribution: inner–outer coordinates. Symbols in table 1.

which results in a peak production of

$$-\overline{u'v'}\left(\frac{\mathrm{d}U}{\mathrm{d}y}\right) = \frac{u_\tau^4}{4\nu}. \tag{3.32}$$

A dashed line figure 26 shows this value, which agrees, within experimental uncertainty, with the peak in the data at $y^+ = 10$.

Assuming that the total shear stress is approximately constant and equal to τ_w in the log region implies that the production should lie along the line

$$-\overline{u'v'}^+\left(\frac{\mathrm{d}U^+}{\mathrm{d}y^+}\right) = \frac{1}{\kappa y^+}. \tag{3.33}$$

This line is plotted in figure 26, and agrees with the data in the log region, with the possible exception of the lowest-Reynolds-number case.

Figure 27 shows the production term of the Reynolds shear stress transport equation, after making the standard boundary-layer approximation, $\partial/\partial y \gg \partial/\partial x$. The peak of $\overline{v'^2}(\partial U/\partial y)$ is lower than the turbulent kinetic energy production peak, and

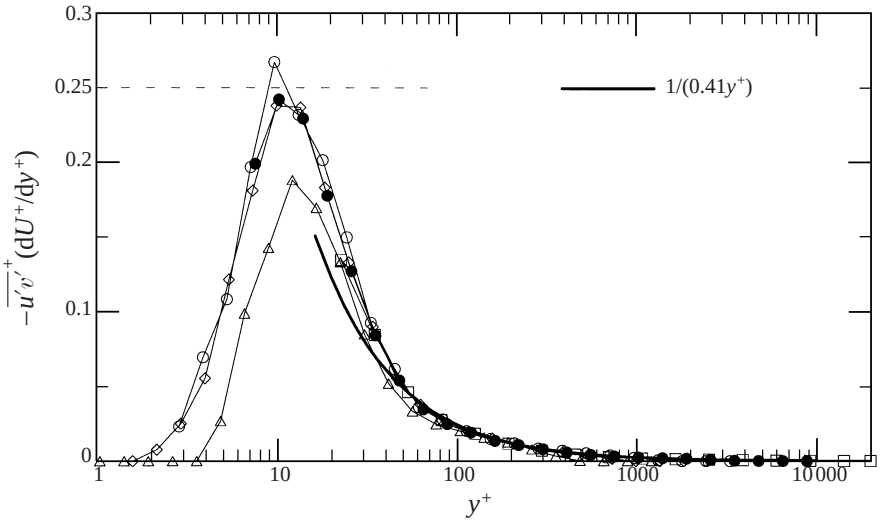

FIGURE 26. Turbulent kinetic energy production. Symbols in table 1. The dashed line indicates the theoretical maximum production.

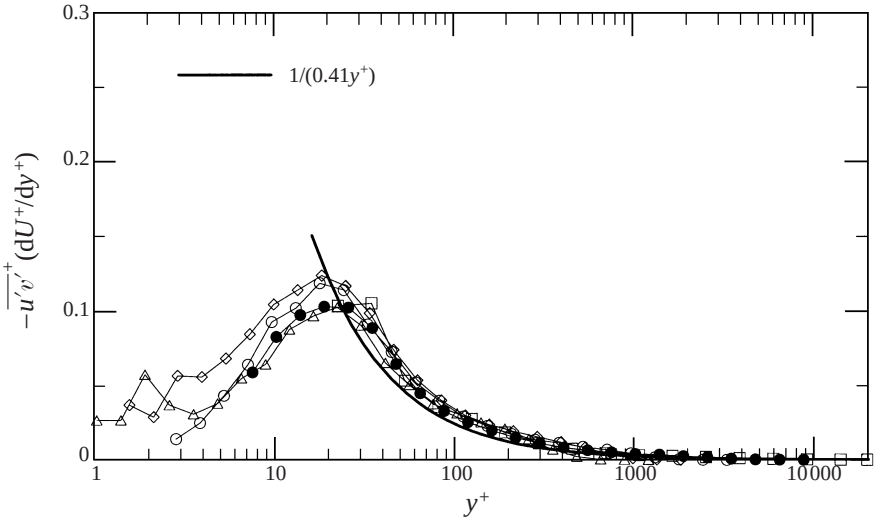

FIGURE 27. Reynolds shear stress production. Symbols in table 1.

centred at $y^+ \approx 20$. The line $(\kappa y^+)^{-1}$ is included for comparison with the $\overline{u'^2}$ production. Since $\overline{v'^2}$ is roughly constant in the log region, the decrease in shear stress production is largely determined by the mean velocity gradient, and therefore parallels the $(\kappa y^+)^{-1}$ behaviour. The scatter in the data for $y^+ < 4$ is due to the multiplication of the uncertainty of the near-wall $\overline{v'^2}$ measurements by the large velocity gradient.

4. Conclusions

The following behaviour defines the equilibrium boundary layer:

(i) The log law collapses the streamwise mean velocity in the inner layer well. Because the wall shear stress was inferred from a log law fit, no firm conclusions

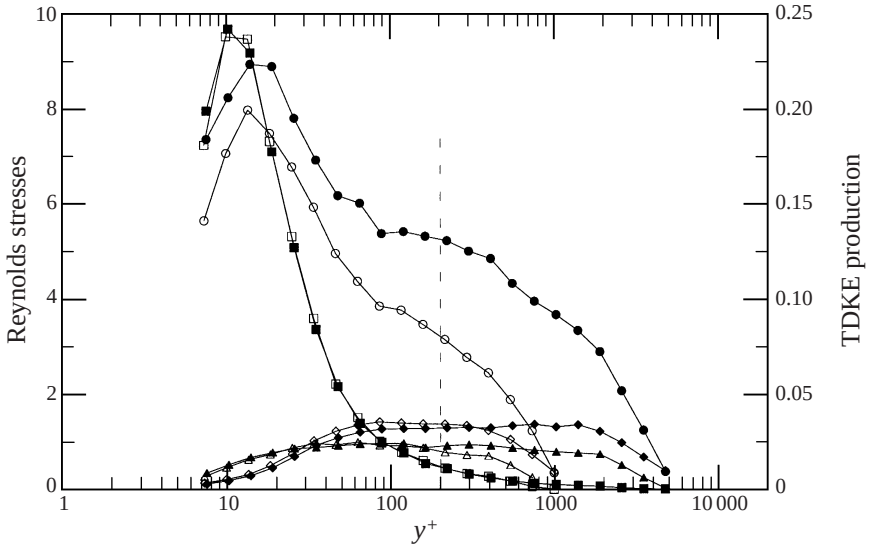

FIGURE 28. Inner region boundary-layer scaling. Open symbols: $Re_\theta = 2900$; solid symbols: $Re_\theta = 13\,000$. ○, $\overline{u'^2}^+$; ◇, $\overline{v'^2}^+$; △, $\overline{u'v'}^+$; □, $\overline{u'v'}^+(\partial U^+/\partial y^+)$. Below the dashed line $\overline{u'v'}^+$ and $\overline{v'^2}^+$ scale on the viscous lengthscale.

can be drawn about the accuracy of the log law from this data. However, since the mean streamwise velocity data collapse well in the sublayer, and since the total shear stress near the wall is near unity, we can conclude that the log law works well for $1430 < Re_\theta < 31\,000$. We can also conclude that any experiment which hopes to resolve log law versus power law controversies must have a very accurate independent measurement of the wall shear stress.

(ii) The streamwise Reynolds stress does not scale on u_τ^2 even in the near-wall region. Remarkably good collapse is attained with the mixed scaling, $\overline{u'^2}^\circ \equiv \overline{u'^2}^+ \sqrt{C_f/2}$, showing a near-wall peak value of approximately 0.32 at $y^+ = 14$.

(iii) The wall-normal Reynolds stress collapses well on the wall shear stress, attaining a plateau value of approximately 1.35 from $y^+ > 90$ to $y/\delta < 0.25$. Above this plateau, $\overline{v'^2}$ decreases approximately linearly.

(iv) The Reynolds shear stress is well collapsed on u_τ, and falls fairly linearly from the wall, although the data are too scattered to establish a definite total shear stress profile shape. The Reynolds shear stress attains a maximum value of approximately 0.95 at $y^+ \approx 70$ for $2000 < Re_\theta < 31\,000$. The lowest-Reynolds-number case shows depressed total shear stress levels, apparently due to low-Reynolds-number or pressure-gradient effects.

(v) The turbulent kinetic energy production collapses well on inner scales. The maximum normalized turbulent kinetic energy production occurs at $y^+ \approx 10$, and has a value of 0.25, consistent with the concept that the total shear stress very near the wall is approximately the same as the shear stress at the wall.

These points are emphasized in figures 28 and 29, which compare just the $Re_\theta = 2900$ case with the $Re_\theta = 13\,000$ case. The lengthscale of the inner region is ν/u_τ, so $\overline{v'^2}^+$, $\overline{u'v'}^+$, and TKE production should collapse in the inner region in figure 28. The dashed line in the figure indicates where $y/\delta = 0.2$ for the lower-Reynolds-number case, and below this line $\overline{v'^2}^+$, $\overline{u'v'}^+$, and the turbulent kinetic energy production

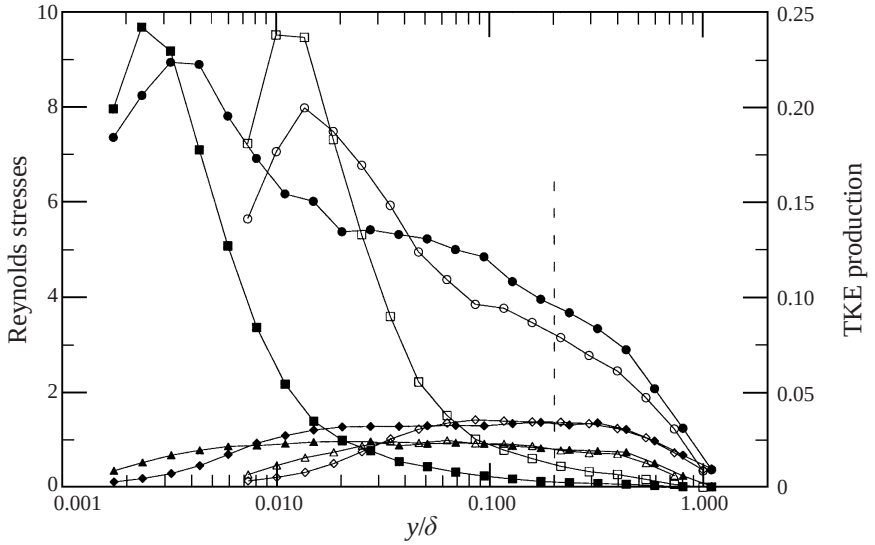

FIGURE 29. Outer region boundary-layer scaling. Symbols as in figure 28. Above the dashed line $\overline{u'v'}^+$ and $\overline{v'^2}^+$ scale on the boundary-layer thickness.

collapse fairly well. The inner region extends to $y^+ = 850$ for the $Re_\theta = 13\,000$ case. It is clear that the two $\overline{u'^2}^+$ profiles do not collapse with Reynolds number. In the outer region, the lengthscale is δ, and figure 29 shows fairly good collapse of $\overline{v'^2}$ and $\overline{u'v'}$ above the dashed line at $y/\delta = 0.2$. Again, $\overline{u'^2}^+$ does not show good collapse.

Contrary to many previous boundary-layer studies, we find that the classic inner/outer scalings proposed by Townsend (1956) are fairly successful in scaling the Reynolds stresses. Provided the momentum-thickness Reynolds number is above approximately 2000, the wall-normal Reynolds stress and Reynolds shear stress collapse fairly well onto Reynolds-number-independent self-similar profiles. The mystery, of course, is the streamwise Reynolds stress, for which empirical evidence suggest the proper scaling is $u_\tau^2\sqrt{2/C_f}$. The authors await further empirical or theoretical evidence of this scaling.

This work was supported by the Office of Naval Research, under grant number N00014-94-1-0070, supervised by Dr L. P. Purtell and Dr C. Wark. The authors would like to thank Professor P. Bradshaw for many useful discussions of boundary-layer scaling.

REFERENCES

ALFREDSSON, P. J., JOHANSSON, A. V., HARITONIDIS, J. H. & ECKELMANN, H. 1988 The fluctuation wall-shear stress and the velocity field in the viscous sublayer. *Phys. Fluids* **31**, 1026–1033.

ANDREOPOULOS, J., DURST, F., ZARIC, Z. & JOVANOVIC, J. 1984 Influence of Reynolds number on characteristics of turbulent wall boundary layers. *Exps. Fluids* **2**, 7–16.

ANTONIA, R. A. & KIM, J. 1994 Low Reynolds number effects on near-wall turbulence. *J. Fluid Mech.* **276**, 61–90.

BARENBLATT, G. I. 1993 Scaling laws for fully developed turbulent shear flows. Part 1: Basic hypotheses and analysis. *J. Fluid Mech.* **248**, 513–520.

BRADSHAW, P. 1967 'Inactive' motion and pressure fluctuations in turbulent boundary layers. *J. Fluid Mech.* **30**, 241–258.

Bradshaw, P. & Huang, G. P. 1995 The law of the wall in turbulent flow. *Proc. R. Soc. Lond.* A **451**, 165–188.

Bruns, J., Dengel, P. & Fernholz, H. H. 1992 Mean flow and turbulence measurements in an incompressible two-dimensional turbulent boundary layer. Nr. 02/92, Technische Universitat Berlin.

Clauser, F. H. 1956 The turbulent boundary layer. *Adv. Appl. Mech.* **4**, 1–51.

Coles, D. 1956 The law of the wake in the turbulent boundary layer. *J. Fluid Mech.* **1**, 191–226.

Coles, D. E. 1962 The turbulent boundary layer in a compressible fluid. *Tech. Rep.* R-403-PR. United States Air Force Project RAND.

DeGraaff, D. B. 1999 Reynolds number scaling of the turbulent boundary layer on a flat plate and on swept and unswept bumps. PhD thesis, Stanford University.

DeGraaff, D. B. & Eaton, J. K. 2000 A high-resolution laser Doppler anemometer: Design, qualification, and uncertainty. *Exps. Fluids* (to appear).

Erm, L. P. & Joubert, P. N. 1991 Low Reynolds-number turbulent boundary layers. *J. Fluid Mech.* **230**, 1–44.

Fernholz, H. H. & Finley, P. J. 1996 The incompressible zero-pressure-gradient turbulent boundary layer: An assessment of the data. *Prog. Aerospace Sci.* **32**, 25–311.

Fernholz, H. H., Krause, E., Nockemann, M. & Schober, M. 1995 Comparative measurements in the canonical boundary layer at $Re_\theta < 6 \times 10^4$ on the wall of the German–Dutch windtunnel. *Phys. Fluids* **7**, 1275–1281.

Gad-el-Hak, M. & Bandyopadhyay, P. R. 1994 Reynolds number effects in wall-bounded turbulent flows. *Appl. Mech. Rev.* **47**, 307–365.

George, W. K. & Castillo, L. 1997 Zero-pressure-gradient turbulent boundary layer. *Appl. Mech. Rev.* **50**, 689–729.

Johansson, A. V. & Alfredsson, P. H. 1983 Effects of imperfect spatial resolution on measurements of wall-bounded turbulent shear flows. *J. Fluid Mech.* **137**, 409–421.

Khoo, B. C., Chew, Y. T. & Li, G. L. 1997 Effects of imperfect spatial resolution on turbulence measurement in the very near-wall viscous sublayer region. *Exps. Fluids* **22**, 327–335.

Klebanoff, P. S. 1955 Characteristics of turbulence in a boundary layer with zero pressure gradient. *Tech. Rep.* 1247. NACA.

Klewicki, J. C., Murray, J. A. & Falco, R. E. 1994 Vortical motion contributions to stress transport in turbulent boundary layers. *Phys. Fluids* **6**, 277–286.

Landau, L. D. & Lifshitz, E. M. 1987 *Fluid Mechanics*, 2nd Edn. Pergamon.

Ligrani, P. M. & Bradshaw, P. 1987 Spatial resolution and measurement of turbulence in the viscous sublayer using subminiature hot-wire probes. *Exps. Fluids* **5**, 407–417.

Mabey, D. G. 1979 Influence of the wake component on turbulent skin friction at subsonic and supersonic speeds. *Aero. Q.* **30**, 590–606.

Marusic, I., Uddin, A. K. M. & Perry, A. E. 1997 Similarity law for the streamwise turbulence intensity in zero-pressure-gradient turbulent boundary layers. *Phys. Fluids* **9**, 3718–3726.

Mochizuki, S. & Nieuwstadt, F. T. M. 1996 Reynolds-number-dependence of the maximum in the streamwise velocity fluctuations in wall turbulence. *Exps. Fluids* **21**, 218–226.

Moffat, R. J. 1988 Describing the uncertainties in experimental results. *Expl Therm. Fluids Sci.* **1**, 3–17.

Moin, P. & Spalart, P. R. 1987 Contributions of numerical simulation data base to the physics, modeling, and measurement of turbulence. *Tech. Rep.* 100022. NASA.

Monin, A. S. & Yaglom, A. M. 1971 *Statistical Fluid Mechanics*, vol. 1. MIT Press.

Osterlund, J. M. 1999 Experimental studies of zero pressure-gradient turbulent boundary layer flow. PhD thesis, Royal Institute of Technology, KTH, Stockholm.

Park, S. R. & Wallace, J. M. 1993 The influence of instantaneous velocity gradients on turbulence properties measured with multi-sensor hot-wire probes. *Exps. Fluids* **16**, 17–26.

Patel, V. C. 1965 Calibration of the Preston tube and limitations on its use in pressure gradients. *J. Fluid Mech.* **23**, 185–205.

Perry, A. E. & Li, J. D. 1990 Experimental support for the attached eddy hypothesis in zero-pressure gradient turbulent boundary layers. *J. Fluid Mech.* **218**, 405–438.

Perry, A. E., Marusic, I. & Li, J. D. 1994 Wall turbulence closure based on classical similarity laws and the attached eddy hypothesis. *Phys. Fluids* **6**, 1024–1035.

Purtell, L. P., Klebanoff, P. S. & Buckley, F. T. 1981 Turbulent boundary layer at low Reynolds number. *Phys Fluids* A **24**, 802–811.

Roach, P. E. & Brierley, D. H. 1989 The influence of a turbulent freestream on zero pressure gradient transitional boundary layer development. In *Numerical Simulation of Unsteady Flows and Transition to Turbulence* (ed. O. Pironneau). Cambridge University Press.

Rotta, J. C. 1962 Turbulent boundary layers in incompressible flow. *Prog. Aeronaut. Sci.* **2**, 1–220.

Spalart, P. R. 1988 Direct simulation of a turbulent boundary layer up to $Re_\theta = 1410$. *J. Fluid Mech.* **187**, 61–98.

Sreenivasan, K. R. 1989 The turbulent boundary layer. *Frontiers in Expl Fluid Mech.* **46**, 159–209.

Tennekes, H. & Lumley, J. L. 1972 *A First Course in Turbulence*. MIT Press.

Townsend, A. A. 1956 *The Structure of Turbulent Shear Flow*. Cambridge University Press.

Townsend, A. A. 1961 Equilibrium layers and wall turbulence. *J. Fluid Mech.* **11**, 97–120.

Townsend, A. A. 1976 *The Structure of Turbulent Shear Flow*, vol. 2. Cambridge University Press.

Zagarola, M. V., Perry, A. E. & Smits, A. J. 1997 Log laws or power laws: the scaling in the overlap region. *Phys. Fluids* **9**, 2094–2100.